Turkish Computational and Theoretical Chemistry

Turkish Comp Theo Chem (TC&TC)

Volume(Issue): 8(2) – Year: 2024 – Pages: 80-100

e-ISSN: 2602-3237

https://doi.org/10.33435/tcandtc.1381982

***Received**: 28.10.2023* ***Accepted**: 24.03.2024* *Research Article*

Investigating the Potential Pharmacological Applications of 5-Hydroxy-2 (hydroxymethyl)-4H pyran-4 one through Electronic Characterization and MM-GBSA Studies for Oxidative Stress and Tyrosinase Inhibition: A Quantum Chemical Approach

Attar Kubaib [a, 1], N. Nadeem Afroze [a], Predhanekar Mohamed Imran [a]

[a] Department of Chemistry, Islamiah College (Autonomous), Vaniyambadi - 635752, Tamilnadu, India

Abstract: The study thoroughly examines the possible applications of 5 Hydroxy – 2 (hydroxymethyl) – 4 H pyran – 4 one. Through Quantum chemical analysis, the research rigorously evaluates the compound's properties, including its optoelectronics, geometrical structure, and intermolecular interactions. The geometrical structure parameters were optimized using a 6–311++G(d,p) basis set in the DFT/B3LYP method, and the resulting geometrical factors were then scaled to calculate probable vibrational wavenumbers. The Mulliken charges and MEP map were used to locate electrophilic, nucleophilic regions, and chemical reactivity was described using FMOs and Fukui function assessments. The multiwfn was employed to investigate topological analysis (surface distance projection and Hirshfeld maps). The UV-visible spectrum was used to estimate the absorption of maximum wavelengths, which was then correlated with the TD-DFT, DOS, and band structure investigations. The study also calculated parameters, including Total Energies, ZPE, Entropy, Dipole moment, and Heat Capacity for monomeric and dimeric units. Pharmacokinetics were used to determine the biological characteristics of the compound. The MM-GBSA simulation was performed, and the results suggest that this compound has the potential to be an enhancing anti-oxidant protection agent due to its high binding affinity and intermolecular interactions. These findings are crucial in developing therapeutic agents with pharmacological effects and potential toxicities.

Keywords: Pharmacological activity, FMO, NBO, Optoelectronics, MM-GBSA profiling, Pharmacokinetics

1. Introduction

Our body is constantly under attack from reactive oxygen species (ROS) during oxidative stress, which can negatively impact cellular function [1]. However, our bodies have developed sophisticated mechanisms to combat these harmful effects. Enzymes like peroxiredoxin 5 (PRDX5) and protein tyrosine kinases (PTKs) play a crucial role in regulating ROS levels and controlling the activity of NADPH (Nicotinamide-Adenine-Dinucleotide-Phosphate) oxidase [2]. By understanding and utilizing these mechanisms, we can help maintain our cellular health and minimize the adverse effects of oxidative stress [3]. It's reassuring to know that we have natural defences against oxidative stress and can further enhance these mechanisms through scientific studies.

Natural bioactive molecules have been extensively studied for their potential to enhance pharmacological applications. Among these, the compound 5 Hydroxy – 2 (hydroxymethyl) – 4 H pyran – 4 one has been proven to have diverse applications across industries such as medicine, dye, cosmetics, and food [4, 5,6]. It is imperative to develop new potent compounds as tyrosinase inhibitors and in this regard, *in-vitro* studies have shown promising results. In addition, this compound is also used as an agrochemical, ovicide, photoinitiator, and insecticide [7].

Analyzing the title compound using the Gaussian 16W and Gauss View 06 package was used to compute and visualize the optimized geometries, fundamental vibrational frequencies, and band intensity, including bond lengths, bond angles,

---

[1] Corresponding Authors

e-mail: attar.kubaib@gmail.com

FMO, NBO, dipole moments, and atomic charges [8]. The UV spectral analyses were conducted using TD-DFT/B3LYP/6-311++G(d,p) basis set [9]. Also, verified calculations of the band gap values are compared and demonstrate good agreement with the VASP calculations and experimental studies. The study also examined non-covalent interactions between molecules using the Multiwfn software.

Incorporating MM-GBSA (Molecular Mechanics Generalized Born Surface Area) simulation is advantageous for complementing experimental findings and understanding the chemical behavior of diverse molecular arrangements. Pharmacokinetics predicts a compound's biological activity through its 2D structural formula, providing valuable insights into a compound's mechanisms of action and potential toxicities as it signifies the pharmacological activity of the compound [10, 11, 12].

The study highlights the potential of the title compound with high binding affinity in developing a novel drug for treatment. Optoelectronic materials, molecules that can generate ROS when exposed to light, could be used as photosensitizers. ROS can be used to kill cancer cells or to inactivate bacteria [13]. Overall, the findings of this study contribute to a better understanding of optical behavior and could have practical applications in various fields.

This study aims to investigate the potential of 5 Hydroxy-2 (hydroxymethyl)-4 H pyran-4 one as a drug to contribute to the development of new potent compounds for anti-oxidant protection and other applications in various industries. The study analyzes the compound's optimized geometries, both experimental and theoretically vibrational frequencies, using Gaussian 16W and Gauss View 06 packages. In addition, UV and NMR spectral analyses, non-covalent interactions, and MM-GBSA simulations have been conducted to predict the compound's pharmacokinetics and potential toxicities.

2. Computational Method

2.1. Experimental Details

The solid compound with a purity of over 98% was acquired by Sigma-Aldrich Chemical Company (USA) and used without further filtration. Characterized by the FT-IR spectrum, it was captured at room temperature within the 400-4000 cm^{-1} range using the KBr pellet method. The experimental FT-IR spectra were then correlated with calculated vibrational studies. In addition, the UV absorption spectrum of the compound, covering a wavelength range of 250-450 nm, was thoroughly examined. The NMR spectra of the compound were then evaluated using a Varian Mercury-VxBB 300 spectrometer in methanol at room temperature (299.95 MHz for ^1H and 75.43 MHz for ^{13}C).

2.2. Quantum chemical calculations

The Gaussian 16W programme [14] has been employed to perform all quantum chemical calculations. VEDA software generates the potential energy distribution (PED) technique assignments [15]. FMOs, Fukui function, Mulliken charges and MEP activities for the gaseous phase were computed using B3LYP with 6–311++G(d,p) as the basis set. NBO analysis has assessed interactions between molecular orbitals and lone pairs, as well as bonds and anti-bonds [16]. By employing the second-order Fock matrix, the NBO analysis investigates the impact of donor and acceptor interactions on stability. It yields the stabilization energy, E(2), and donor (i) - acceptor (j) interaction for each interaction, also known as donor-level bonds to acceptor-level bonds. When assessing the stabilization energy E(2), it's vital to consider various factors such as the occupancy of the donor orbit (qi), diagonal elements (εj and εi), and the off-diagonal NBO Fock matrix component, which is known as F(i, j) [17].

$$E(2) = \Delta E_{ij} = q_i \frac{F(i,j)^2}{\varepsilon_j - \varepsilon_i}$$

Electronic excitation simulated UV–visible spectrum was procured using TD-DFT method B3LYP with 6–311++G(d,p) as the basis set. A few thermodynamic and electronic characteristics [18], such as SCF energy, zero-point, vibrational energy, dipole moment (D), Entropy (S), and Heat Capacity (Cv) in gas with dimeric units [19], have also been calculated using the B3LYP approach. Topology studies were conducted using the Multiwfn 3.8 [20] analysis tool to identify hydrogen bonding effectively, van der Waals interactions and steric effects.

To study the electronic levels and band gap, also correlated in the present study, first-principles calculations based on density functional theory using the Vienna Ab initio Simulation package (VASP) were employed. To execute these calculations using the MedeA program [21] and the projector-augmented wave (PAW) pseudopotential, the generalized gradient approximation of the Perdew–Burke–Ernzerhof (PBE-GGA) method was implemented. A plane-wave basis set with a 400 eV cut-off energy was employed. The optimization process involved a 5 × 5 × 1 Monkhorst–Pack k-mesh in the Brillouin zone.

MM-GSA simulations to create models of organic materials, which allowed us to sample the local dimer charge hopping rates throughout the system. Alao revealed that the compounds were the most effective based on the dock ranking and the number of hydrogen bond interactions. It had a favorable binding energy supporting efficient receptor modulation with Targeting 1HD2, 3H4K and 3AL4 proteins aimed to gain insights into their interactions with our ligands and explore potential activity modulators [22]. Protein Preparation Wizard is utilized to optimize, preprocess and minimize our proteins. Our mono and dimeric units (ligand) structures were then imported into the Gaussian 16W program to create the ligand compounds for subsequent docking analysis. Using the OPLS 2005 force field, optimized ligands and protein generated a 30x30x30 grid on our protein receptors. The resulting protein-grid output file was then used to investigate the docking of our ligands using the Glide SP (standard precision) module of the Schrodinger Maestro software [23]. The molecular docking process is utilized to forecast the behavior of protein-ligand complexes. It involves two main elements: a scoring function that evaluates the binding affinity of the ligand to the protein based on their complex geometry and a search algorithm that generates potential protein-ligand complex geometries. Calculating the binding energies of a ligand is a standard method for determining its binding affinity. The highest binding energy was obtained from the docking results in this investigation, and the Discovery Studio Visualizer was utilized to examine the remaining interactions.

The pharmacokinetic parameters were determined using a canonical simplified molecular input line entry system (SMILE). The compounds' absorption, distribution, metabolism and elimination (ADME) properties were also predicted using SwissADME tool software [24]. The ADME study indicates the lipophilicity, physicochemical properties, drug-likeness and toxicity of compounds. This tool uses 2D and 3D descriptors and bioactive ligand models to establish structure-activity connections [25].

This study utilized the Schrödinger Materials Science Suite (MSS) 2018-1 [26] to conduct an optoelectronic molecule analysis with the Jaguar, Desmond, and Maestro programs by the OPLS3 force field [27]. To determine organic electronic efficiency, which depends on charge mobility and charge injection.

$$D = l^2 k_{ET}$$

$$\mu_{hop} = eD/k_B T$$

Assess these properties following the hopping mechanism to describe how charge carriers move from one molecule to another. The hopping mechanism's rate constant of charge transport between molecules, k_{ET}, can be found in the expression for the diffusion coefficient, D. To maximize the rate of charge transport, we need to minimize the reorganization energy (λ) and maximize the charge transfer integral (t).

Our findings provide valuable insights into charge transport mechanisms and could significantly impact the development of organic electronics and other fields [28]. Our analysis also identified intramolecular interactions in the compound, which has prompted a closer investigation of its potential pharmacological applications.

3. Results and discussion

3.1. Molecular Geometry

The study evaluated theoretical bond parameters at the B3LYP/6-311++G(d,p) method. Based on bond lengths within the molecular system, the analysis provides valuable insights into the distances between atoms, reflecting their interactions and stability. As shown in Figure 1 and Table S1, involved in consistency in Hydrogen bonds such as O10-H16 and O8-H15 exhibit consistent bond lengths of 0.97 Å, indicating stable hydrogen bonding interactions. C4-H12 and C1-H11 also share uniform bond lengths of 1.08 Å, suggesting a stable environment for these atoms. In Carbon-Carbon bonds, C6-C7 and C1-C2 exhibit longer bond lengths of 1.50 Å, indicative of a potential double bond character. C3-C4 and C2-C3 maintain slightly shorter bond lengths at 1.35 Å, signifying strong carbon-carbon interactions. In Oxygen-Carbon bonds, C7-O8 and C4-O5 demonstrate consistent bond lengths of 1.43 Å and 1.36 Å, respectively, suggesting stable oxygen-carbon interactions. As in Oxygen-Oxygen bonds, O5-C6 and O10-H16-C3-C2 show stable bond lengths at 1.35 Å, reflecting well-defined oxygen-oxygen interactions within the molecular system.

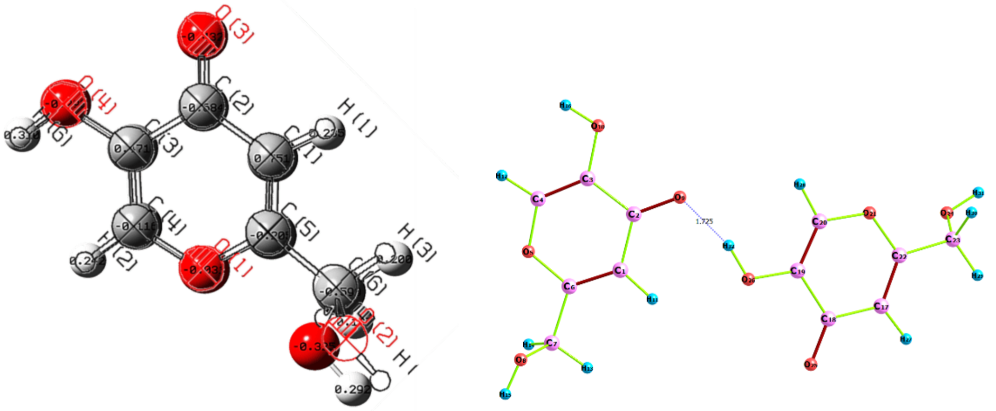

Figure 1. Monomer and dimeric optimized structures obtained by B3LYP/6-311++G(d,p) basis set

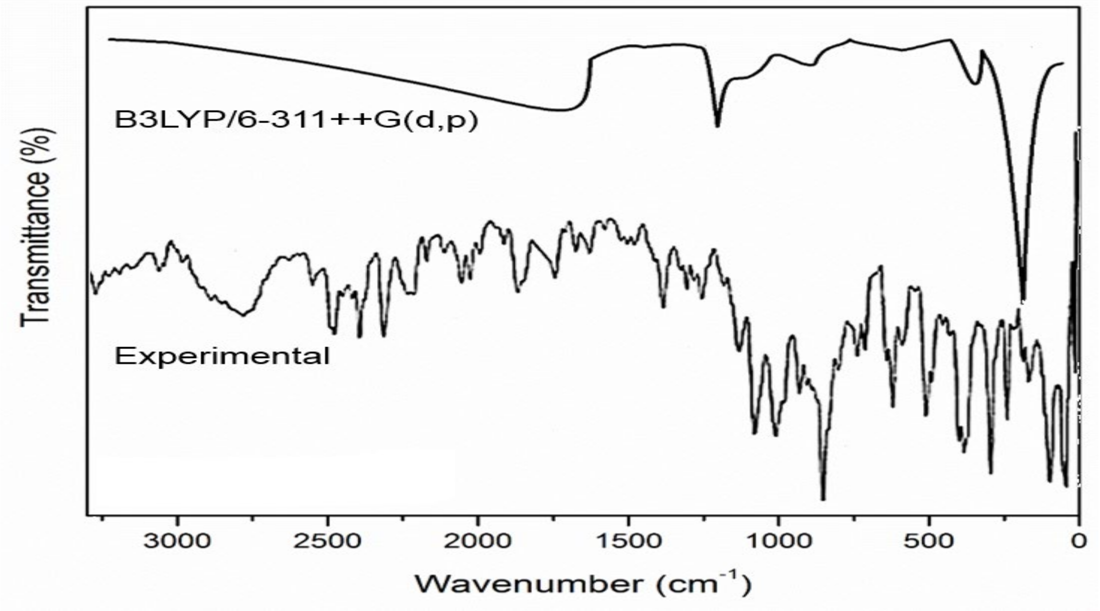

Figure 2. Comparison of the observed and computed FT-IR spectra

Analysis based on bond angles provides crucial information about the molecular geometry and spatial arrangement of atoms. Key observations include the planarity of Carbon atoms. C6-C7-O8 and O5-C6-C1 exhibit planar bond angles of 108.56°, suggesting a flat molecular configuration. C1-C2-O9 maintains a planar angle of 115.89°, contributing to a linear arrangement. Analysis based on dihedral angles captures the spatial orientation of planes formed by four consecutive atoms. Essential observations include conformational stability. O10-C3-C4-O5 and C2-C3-C4-H12 exhibit dihedral angles of 179.70° and -0.01°, indicating stable conformations within the molecular system. C4-O5-C6-C1 and C2-C3-C4-O5 display dihedral angles close to 0°, suggesting a coplanar arrangement. Conformational flexibility represented in C6-C1-C2-O9 and C2-C1-C6-C7 demonstrates dihedral angles of 179.02° and -1.04°, reflecting the conformational flexibility of these molecular fragments. The detailed analysis based on bond lengths, bond angles, and dihedral angles provides a comprehensive understanding of the molecular system. The identified structural features contribute to our insights into the system's stability, geometry, and potential reactivity, laying the groundwork for further investigations into its dynamic behavior and applications in various scientific disciplines.

3.2. Vibrational Spectral Analysis

The FT-IR spectra were analyzed using theoretical wavenumbers to determine their vibrational spectra. A comprehensive list of the 42 fundamental vibration modes commonly found in molecules is available in Figure 2 and Table 1. Comparing the estimated wavenumbers to the experimental values [29] showed that they agreed with the experimental observations. The intensities of vibrational modes in the dimer appear higher in some cases than in the monomer. It suggests that specific vibrational modes become more pronounced in the dimer, indicating molecular interactions or dipole moment changes.

In examining the vibrational frequencies of both the monomeric and the dimeric compound, νOH (Hydroxyl Stretching) modes at 3826.73 cm^{-1} and 3799.57 cm^{-1} (monomer) and 3845.74 cm^{-1}, 3842.35 cm^{-1} and 3820.66 cm^{-1} (dimer) fall within the typical range of 3500-3200 cm^{-1}, confirming the presence of hydroxyl groups [30]. The minor variations could arise from hydrogen bonding effects, influencing the stretching frequencies of hydroxyl groups. The νCH (Methyl and Methine Stretching) modes at 3224.11 cm^{-1} and 3208.89 cm^{-1} (monomer) and 3220.18 cm^{-1}, 3206.93 cm^{-1}, 3204.31 cm^{-1} and 3202.13 cm^{-1} (dimer) align with the anticipated range of 3100-3000 cm^{-1} [31], indicating the presence of methyl and methine groups, this discrepancy may stem from factors influencing the potential interactions with neighboring functional groups. The νCH (Aromatic C-H Stretching) mode at 3074.07 cm^{-1} (monomer) and 3057.57 cm^{-1} (dimer) deviates slightly from the typical range of 3100-3000 cm^{-1} but still indicates the presence of aromatic structures. The νCH (Aliphatic C-H Stretching) mode at 3025.10 cm^{-1} (monomer) and 3050.42 cm^{-1} (dimer) falls within the expected range, signifying aliphatic C-H stretching vibrations. Examining the νOC (Carbonyl Stretching) modes at 1670.50 cm^{-1} and 1499.32 cm^{-1} (monomer) and 1709.41 cm^{-1}, 1687.62 cm^{-1}, and 1666.46 cm^{-1} (dimer), the observed values align well with the typical ranges of 1750-1650 cm^{-1} and 1800-1650 cm^{-1}, confirming the presence of carbonyl functionalities. Variations in these stretching frequencies could arise from the specific nature of the carbonyl groups and their conjugation within the molecular structures. Finally, the νCC (C=C Stretching) modes at 1644.67 cm^{-1}, 1625.84 cm^{-1} (monomer) and 1658.48 cm^{-1}, 1634.02 cm^{-1}, and 1630.51 cm^{-1} (dimer) fall within the expected range of 1700-1600 cm^{-1}, indicating the existence of carbon-carbon double bonds. In summary, the observed vibrational frequencies generally align with the experimental ranges. Analyzing these deviations provides valuable insights into the intricacies of the conformational effects within both the monomeric unit and the dimeric compound and the factors influencing vibrational behavior.

Table 1. The observed and computed vibrational frequencies by using the B3LYP/6-311++G(d,p) method

Freq. scaled (cm^{-1})	**Computed at B3LYP/6-311++G(d,p)**		**Assignments and PED (%)**	**Observed Freq. FT-IR (cm^{-1})**	**Red. Mass (amu)**	**Force Const. (mdyn/Å)**
	Intensity					
	IR	**Raman Km/mol**				
3826.73	92.32	293.38	100 νOH			
3799.57	147.83	211.39	100 νOH			
3224.11	8.43	251.80	99 νCH			
3208.89	0.77	184.47	99 νCH			
3074.07	39.80	138.98	75 νCH	3175w	1.09	6.58
3025.10	53.18	362.46	25 νCH	3094w	1.11	6.40
1670.50	891.66	389.16	34 νOC			
1644.67	1837.74	114.96	65 νCC	1639w	7.86	12.3
1625.84	320.65	97.90	17 νCC			
1499.32	9.24	16.61	90 νOC			
1468.34	127.50	5.76	10 νCC			
1446.27	126.29	11.42	-21 νOC			

1405.33	111.19	16.75	23	νOC			
1310.42	42.86	6.34	10	νCC			
1267.95	131.87	20.31	-21	νOC			
1244.21	105.35	17.90	24	βCCO			
1238.36	166.93	5.85	25	βHOC			
1203.71	1379.42	10.35	-42	βHOC			
1171.14	102.93	49.44	-21	βHCC	1189ms	11.89	1.31
1140.82	987.35	4.02	27	βHCO			
1034.90	346.78	18.22	67	βHCO			
1014.28	66.76	6.81	-20	βHCH			
923.50	484.80	5.69	30	βOCC			
880.69	398.03	0.23	-66	βCCO			
854.92	56.76	8.03	76	βCOC			
783.55	135.55	5.28	-14	βCCC	630ms	0.46	7.12
763.18	8.66	2.77	-13	βOCC			
751.04	63.94	32.61	12	βCCO			
684.06	95.14	10.43	-11	βOCC			
589.43	179.16	15.85	-12	τHOCC			
534.22	136.91	10.51	-14	τHOCC			
457.38	16.31	2.01	-23	τHCCC	456w	10.30	3.22
427.06	18.59	2.09	14	τHCOC			
391.35	240.25	4.33	-15	τHCCC			
332.58	1354.51	1.56	58	τHCCC			
324.28	182.02	2.71	-13	τCCOC			
302.13	453.20	0.37	26	τCCOC			
256.13	105.92	0.92	30	τCCCO			
187.42	4162.84	2.26	97	τOCCC			
160.01	120.16	1.69	-14	αOCCC			
98.02	458.32	0.99	-47	αOCCC			
57.46	384.36	3.02	72	αCCOC			

The scaling factor is around 0.98, and where ν–Stretching; β–in-plane-bending; α–out-of-planebending; s-strong, m-medium, w-weak, ms-medium strong, vs-very strong.

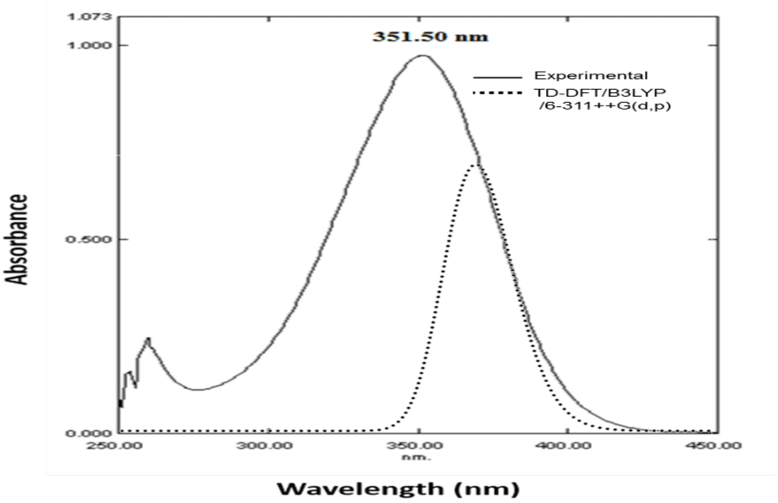

Figure 3. Correlation between observed UV-visible spectrum and TD-DFT method

3.3. UV-Visible Spectral Analysis

In this analysis, we examine the UV spectrum of the title compound and the maximum expected absorption in the visible range, depending on electron availability, presented in Table 2. Using TD-DFT calculations based on a fully optimized ground-state structure, we determined the excited states of this molecule. The system's configurations are evident in the calculations, with transitions involving molecular orbitals in the compound. We then applied the Frank-Condon principle to compare the calculated wavelength and vertical excitation energies with experimental measurements to determine the highest absorption peaks in the UV-visible spectrum. The oscillator strength (f - 0.2734) provides information about the intensity of the electronic transition, with higher values indicating stronger transitions.

The wavelength was obtained at 379.59 nm, which is very close to the experimental value of 351.50 nm listed in Table 2, and Figure 3 shows the strong electronic transition predicted by TD-DFT. The primary change involves nonbonding molecular orbital (n) transitions to antibonding orbital (π*) transitions due to the molecule's oxygen lone pairs. The highest absorption in this molecule is caused by an electron moving from one frontier orbital to another, such as from HOMO to LUMO, as determined by MO geometry calculations. This study suggests that the title compound plays a significant role in electronic transitions.

Table 2. Experimental and Calculated electronic absorption spectrum using TD-DFT/B3LYP/6-311++G(d,p) method

Excitation	CI expansion coefficient	Energy gap (eV)	Wavelength (nm) Calc.	Wavelength (nm) Expt.	Oscillator Strength (f)
Excited-state 1					
43 → 45	**0.6690**	**4.0854**	**407.79**	**351.50**	**0.0033**
Excited State 2					
44 → 45	**0.6474**	**4.1870**	**379.59**	**351.50**	**0.2734**
Excited State 3					
39 → 45	**0.6768**	**4.4699**	**308.20**	**351.50**	**0.0006**

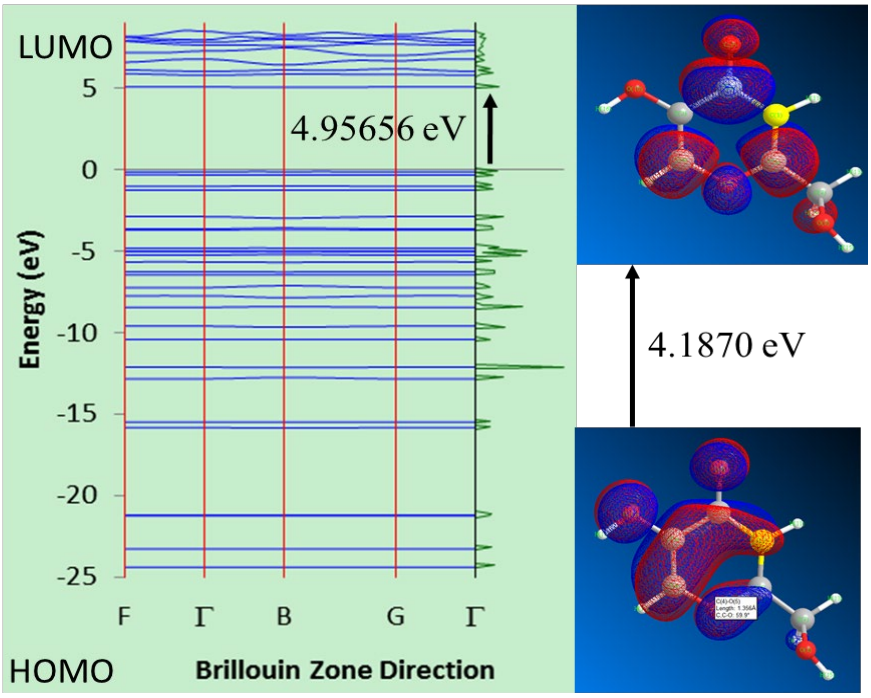

Figure 4. The optimized structure of the title compound, along with the band structure and total density of states with F-Γ-B-G- Γ path

Our study found a calculated band gap of 4.95656 eV in the title compound, aligning remarkably well with theoretical predictions and experimental data. Band structure and DOS suggest that the compound shares similar properties with the title compound. In Figure 4, we present a visual representation of the electronic band structure of the title compound. The graph highlights the principal directions of the Brillouin zone and reveals a zero gap at the K-point. This behavior in the drug is significant.

3.4. Analysis of NMR Spectra

In the analysis of the NMR spectra for the compound, computed chemical shifts at the B3LYP/6-311++G(d,p) level were compared with experimental values to elucidate structural insights [32]. The carbonyl group (C=O) exhibited a computed ^{13}C chemical shift of 178.06 ppm, while the observed value is around 200 ppm. The hydroxyl carbon (C-OH) displayed a computed ^{1}H chemical shift of 3.98 ppm and a ^{13}C shift of 152.68 ppm, with experimental values of 1-5 ppm and 60-80 ppm, respectively. Aromatic protons and carbons showed good agreement between computed and observed values: 7.91 ppm and 171.73 ppm, 6.48 ppm and 144.52 ppm, 121.69 ppm (computed) versus experimental values of 7-8.5 ppm and 115-140 ppm for aromatic protons and carbons, respectively. Methylene (CH_2) displayed a calculated ^{1}H chemical shift of 4.75 ppm and a ^{13}C shift of 66.57 ppm, with experimental values around 1.5-2.5 ppm and 20-40 ppm for methylene protons and carbons, respectively. The hydroxymethyl group (CH_2-O-H) exhibited a computed ^{1}H chemical shift of 1.17 ppm, presented in Table 3, proving the reliability of the NMR predictions for a more robust structural interpretation.

Table 3. Experimental and theoretical ^{1}H, ^{13}C isotropic chemical shifts (concerning TMS)

Atoms	Computed at B3LYP/6-311++G(d,p) (ppm)	Experimental (ppm)
C=O	178.06 (C)	180.01 (C)
C-OH	3.98 (H) 52.68 (C)	4.99 (H) 69.22 (C)
Aromatic	6.48 (H) 7.91 (H)	7.42 (H) 8.15 (H)
Protons/Carbons	121.69 (C) 144.52 (C) 171.73 (C)	124.21 (C) 125.75 (C)
CH2	4.75 (H) 4.43 (H) 66.57 (C)	4.90 (H)
CH2-O-H	1.17 (H)	3.61 (H)

Table 4. GCR Descriptors calculated by DFT B3LYP/6-311++G(d,p) method

Parameters	Monomer	Dimer
Electronic Properties		
E_{HOMO} (eV)	-7.31	-7.19
E_{LUMO} (eV)	-0.11	-0.611
Energy Gap (Eg) (eV)	7.201	6.576
VASP (eV)	5.782	4.957
Electronegativity (χ)	3.711	3.899
Chemical Potential (μ)	-3.711	-3.899
Quantum Chemical Indices		
Global Hardness (η)	0.139	0.152
Chemical Softness (S)	3.601	3.288
Electrophilicity Index (ω)	1.912	2.311
Polarizability	114.02	233.6

Table 5. Second-order perturbation theory analysis of Fock matrix in NBO basis

Donor (i)	Type	ED/e	Acceptor (j)	Type	ED/e	E(2)^a (kJmol^{-1})	E(j)-E(i)^b (a.u)	F(i,j)^c (a.u)
C1-C6	σ	1.98	C1-C2	σ*	0.02	3.22	1.27	0.06
			C2-H7	σ*	0.01	2.32	1.18	0.05
			C5-C6	σ*	0.02	2.86	1.28	0.05
C1-C6	π	1.63	C2-C3	π*	0.01	16.37	0.29	0.06
			C4-C5	π*	0.02	22.54	0.28	0.07
C2-C3	σ	1.97	C1-C2	σ*	0.02	3.45	1.25	0.06
			C1-S11	σ*	0.03	4.52	0.90	0.06
			C3-C4	σ*	0.02	2.48	1.25	0.05
			C4-N16	σ*	0.09	4.02	0.99	0.06
C2-C3	π	1.66	C1-C6	π*	0.03	22.45	0.27	0.07
			C4-C5	π*	0.02	17.88	0.27	0.06
			C4-C5	π*	0.40	4.12	1.07	0.06
C4-C5	σ	1.98	C3-C4	σ*	0.02	4.32	1.26	0.07
			C5-C6	σ*	0.02	2.36	1.27	0.05
			N16-O18	σ*	0.09	2.56	0.96	0.05

C4-C5	π	1.64	C1-C6	π*	0.03	17.09	0.28	0.06
			C2-C3	π*	0.01	21.15	0.29	0.07
			N16-O17	π*	0.03	24.64	0.16	0.06
LP(1)O11		1.98	C1-C6	σ*	0.03	4.44	1.14	0.06
			C12-H13	σ*	0.01	0.62	1.00	0.02
			C12-H14	σ*	0.02	0.70	1.00	0.02
LP(2)O11		1.83	C1-C2	π*	0.02	1.29	0.79	0.03
			(1)C1-C6	π*	0.03	0.65	0.79	0.02
			(2)C1-C6	π*	0.40	16.11	0.25	0.06
LP(1)O17		1.98	C4-N16	σ*	0.09	4.89	1.08	0.07
LP(2)O17		1.87	C4-N16	σ*	0.09	12.95	0.58	0.08
			N16-O18	σ*	0.09	25.38	0.54	0.11
LP(1)O18		1.99	C4-N16	σ*	0.09	3.52	1.12	0.06
			N16-O17	σ*	0.03	1.58	1.32	0.04
LP(2)O18		1.93	C4-N16	σ*	0.09	6.78	0.55	0.06
			N16-O17	σ*	0.58	10.33	0.76	0.08
LP(3)O18		1.52	N16-O17	π*	0.58	94.13	0.13	0.10

[a] E(2) means the energy of hyperconjugative interaction (stabilization energy)

[b] E(j)-E(i) Energy difference between donor and acceptor i and j NBO orbitals.

[c] F(i,j) is the Fork matrix element between i and j NBO orbitals.

3.5. GCRD Analysis

Frontier orbitals, such as the HOMO and LUMO orbitals in quantum chemistry, significantly impact a molecule's interactions. The outermost HOMO orbital is responsible for donating electrons, while the innermost LUMO orbital accepts them [33]. Table 4 provides information on the GCRD (Global Conceptual Density-Functional Theory Reactivity Descriptors). The monomer exhibits an E_{HOMO} of -7.310 eV and an E_{LUMO} of -0.110 eV, resulting in an energy gap (E_g) of 7.201 eV. This substantial energy gap indicates the monomer's relative stability. The χ is calculated as 3.711 eV, and the μ is -3.711 eV, illustrating a balanced electron density distribution.

Upon dimerization, a noteworthy decrease in the E_{HOMO} to -7.190 eV and the E_{LUMO} to -0.611 eV leads to a reduced energy gap of 6.576 eV. A shift from HOMO to LUMO over the C=O group leads to an ED transfer to an electron-deficient group and ring. Figure 4 depicts the atomic compositions of the frontier MOs. The increase in electronegativity to 3.899 eV and a corresponding decrease in chemical potential to -3.899 eV signify changes in the electronic structure upon dimer formation. The η and S values provide information about the system's resistance to changes and its response to external perturbations, with values of 0.139 and 3.601 eV for the monomer and 0.152 and 3.288 eV for the dimer, respectively.

The ω reflects the system's tendency to accept electrons, decreasing from 1.912 eV in the monomer to 2.311 eV in the dimer, indicating an enhanced electrophilic character upon dimerization. The polarizability values also exhibit a significant rise from 114.02 to 233.60, signifying an increased ability of the system to undergo electronic distortions in response to external electric fields.

3.6. NBO Analysis

The NBO analysis of the studied molecule reveals a complex network of intra- and intermolecular interactions. Strong sigma (σ) interactions between C1-C6 and C1-C2, as well as C2-C3 with C1-C2 and C3-C4, are characterized by substantial electron density (ED/e) values of 1.98 and 1.97-1.98, respectively, and significant second-order perturbation energies E(2) ranging from 2.32 to 4.52 kJ/mol. In contrast, pi (π) interactions, such as C1-C6 with C2-C3 and C4-C5, exhibit varying electron densities (1.63-1.97) and E(2) values spanning 4.12 to 22.45 kJ/mol, highlighting a spectrum of strengths. Remarkably, the lone pair (LP) interaction involving LP(3)O8-H15 stands out with an exceptionally high E(2) value of 94.13 kJ/mol. This study signifies a pronounced contribution to stabilization, indicating a strong influence on the molecular structure. Overall, the NBO analysis provides a nuanced perspective on the electronic structure, emphasizing both subtle and substantial contributions of stabilizing interactions within the molecule, thus forming a robust foundation for understanding its reactivity and behavior [34].

3.7. Molecular Electrostatic Potential

Understanding the processes of molecule recognition is vital in comprehending interactions between drugs and receptors or enzymes and substrates. The electrostatic potential V(r) plays a crucial role in this analysis, making the Molecular Electrostatic Potential (MEP) tool [35]. These descriptors closely relate to identifying regions of compounds suitable for electrophilic and nucleophilic reactions and hydrogen bond interactions [36]. Predicting the reactive sites for electrophilic and nucleophilic attacks on the studied compounds is essential in drug design, and the optimal geometry of MEP helps achieve this. As depicted in Figure 5, MEP's negative regions are associated with nucleophilic reactivity, while the positive ones relate to electrophilic reactivity. It's worth mentioning that a positive charge covers the carbonyl group, while the hydroxyl hydrogen group is covered by a negative charge, making the molecule highly reactive with higher electronegativity in the hydroxyl group. This insight can help design new drugs that target specific regions of molecules.

3.8. Surface distance projection and Hirschfeld maps

The Multiwfn program was used to generate the Surface Distance projection and Hirschfeld maps, and Figure 6 displays the various interactions in monomers. The validation of topological parameters was thoroughly conducted using the surface distance projection map and Hirshfeld graphs to confirm the chemical concepts derived from the color-code system [37, 38]. The surface distance projection map and Hirshfeld graphs unequivocally indicate that the green carbon region suggests a high probability of interaction between the molecules, representing a highly delocalized electron density in Figure 6. Moreover, the red coloration surrounding hydrogen atoms exemplifies the nature of electron localization in bonding regions. The analysis revealed that the inner space of localized orbitals (red) has a higher value than the boundary region (blue), pointing to electron densities above the upper limit. These topological analyses strongly suggest that the molecule contains strong, active interactions.

3.9. Mulliken Charges

The atomic charge data provides crucial information about electron density distribution in monomeric and dimeric forms within the studied molecular system. In the monomer, notable atomic charges include positive charges on carbon atoms (C1, C3, C6, C7) ranging from 0.4709 to 0.7512, indicative of a partial loss of electron density. Negative charges are observed on oxygen atoms (O5, O8, O9, O10), ranging from -0.0309 to -0.4319, suggesting a partial gain of electron density. Hydrogen atoms (H11 to H16) exhibit positive charges, reflecting their electron-donating nature [39].

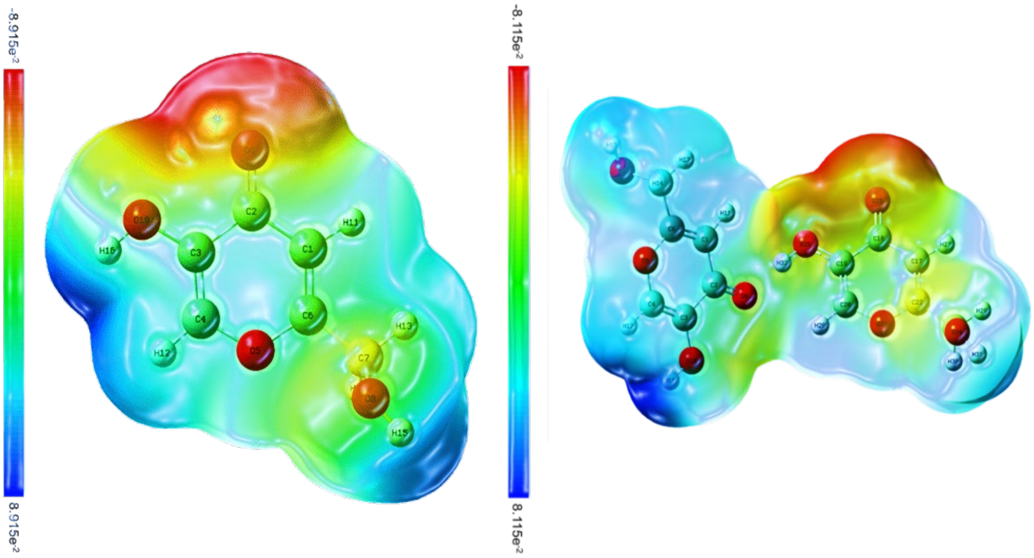

Figure 5. MEP surface view for the monomeric and dimeric units

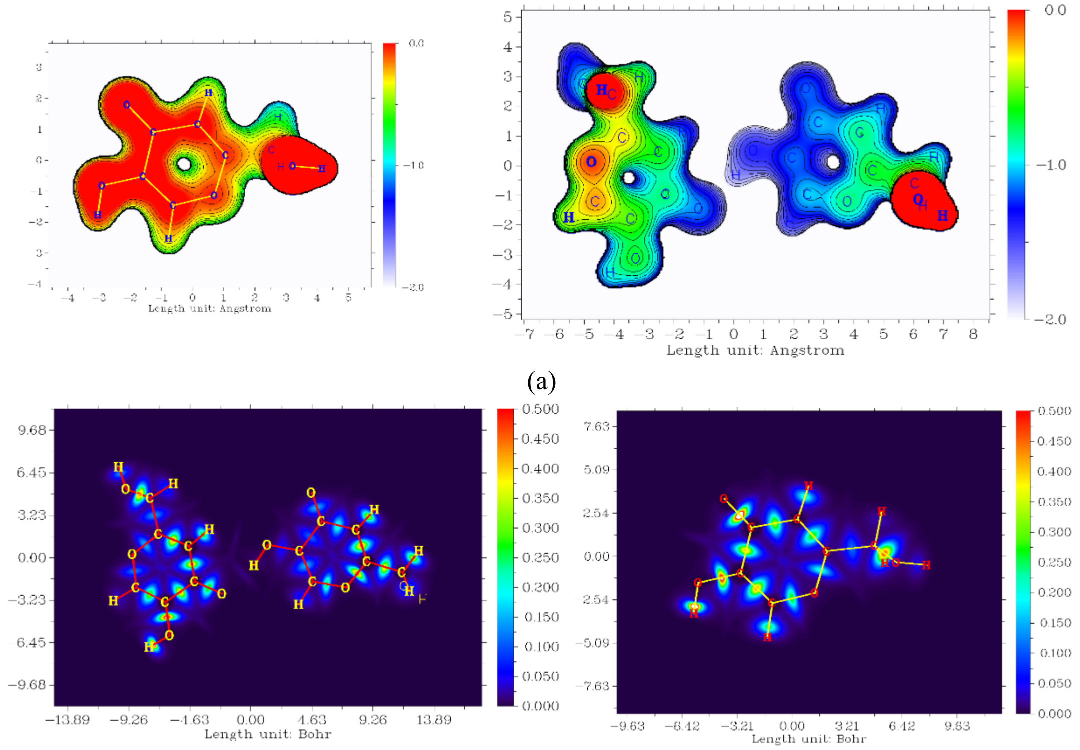

(a)

(b)

Figure 6. (a) Surface distance projection and (b) Hirschfeld map of the title compound

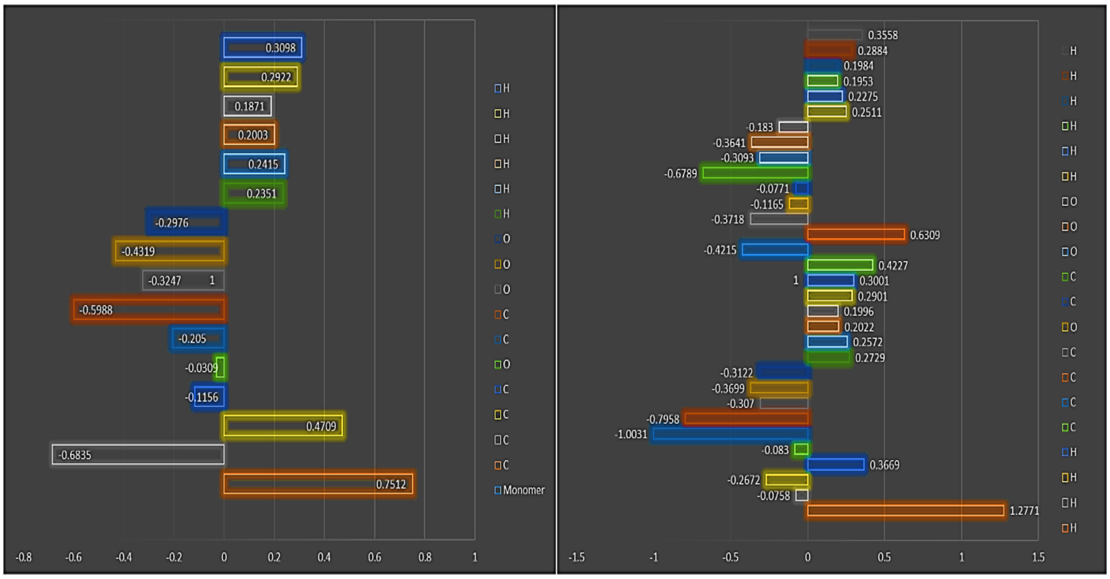

Figure 7. Mulliken charges Chart calculated by B3LYP/6-311++G(d,p) method

Upon dimerization, significant changes in atomic charges are observed. Carbon atoms (C17, C18, C19, C20, C22, C23) in the dimer show positive charges, while carbon atoms (C21, C24) display negative charges. Oxygen atoms (O21 to O26) exhibit varying degrees of negative charges. Hydrogen atoms in the dimer (H27 to H32) remain positively charged, consistent with their electron-donating nature.

Comparing monomeric and dimeric atomic charges reveals alterations in electron distribution upon dimer formation. Notably, the positive charge on C1 in the monomer becomes more pronounced in the dimer (C17). The negative charge on O5 in the monomer also intensifies in the dimer (O21). These changes in atomic charges suggest a redistribution of electron density during the dimerization process, which can impact the molecule's reactivity and interactions with its surroundings, as shown in Figure 7.

3.10. Thermodynamic Properties

Table 6 displays the total energy of the monomer and dimer, measured and found to be -533.28 a.u and -1066.57 a.u, respectively. The zero-point energies increased from 79.15 kcal/mol in the monomer to 160.31 kcal/mol in the dimer, indicating that the dimeric form is more thermodynamically stable. Entropy values also significantly increased from 94.52 cal/mol/K to 156.73 cal/mol/K, further highlighting the increased disorder in the dimeric state.

Table 6. Theoretically computed thermodynamics parameters by B3LYP/6-311++G(d,p) method

Parameters	Monomer	Dimer
Total Energies (a.u)	-533.28	-1066.57
Zero-point Energy (kcal/mol)	79.15	160.31
Entropy (cal/mol/K)	94.52	156.73
Dipole Moment (D)	8.1	11.9
Heat Capacity (Cv) (cal/mol/K)	33.85	71.92
Rotational Constants (GHz)	3.21	3.12
	0.46	0.46
	0.41	0.4
Translational	41.28	41.28
Rotational	30.66	30.71
Vibrational	27.2	29.31

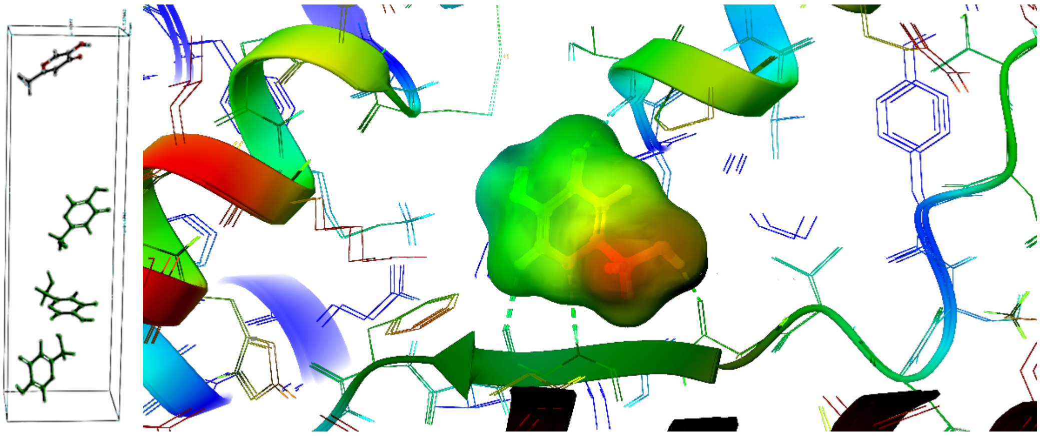

Figure 8. MM-GBSA simulations show adsorption between inter (ligand-receptor) and intra-molecular (mono & dimeric units)

The dipole moment was enhanced from 8.10 Debye in the monomer to 11.90 D in the dimer, suggesting an increase in molecular polarity upon dimerization. Heat capacity values significantly increased from 33.85 cal/mol/K in the monomer to 71.92 cal/mol/K in the dimer, indicating a higher energy requirement for temperature changes in the dimeric state.

Rotational constants showed understated variations between the monomer and dimer. Moreover, translational, rotational, and vibrational contributions to the system's motion were also assessed, providing a comprehensive understanding of the molecular system's dynamic behavior [40].

The adsorption process, illustrated in Figure 8 for the title compound, involves a noteworthy absorption of 23.148166 kcal/mol by the adsorbate. This positive value indicates an endothermic process, suggesting that external energy is absorbed during adsorption. The adsorbate energy, a critical thermodynamic indicator, provides valuable insights into the energetic aspects of adsorption.

The favorable Adsorption Energy of -18.747438 kcal/mol highlights the overall stability of the adsorption complex. These findings contribute to our understanding of adsorption thermodynamics, offering insights for optimizing conditions in applications like binding and interaction with receptors. The positive adsorbate energy emphasizes the role of external energy sources and underscores the importance of considering temperature and environmental factors in designing and analyzing adsorption systems.

The positive adsorbate energy suggests that the adsorption process is energetically favorable, involving energy absorption from the surroundings. This finding is significant for understanding the overall thermodynamics of the adsorption process and can help design and optimize adsorption-based applications.

3.11. Fukui function analysis

Analyzing Fukui function values of individual atoms provides valuable insights into molecular reactivity, which can aid in predicting reactive sites for chemical transformations [41]. The findings from the data suggest certain atoms exhibit significantly higher Fukui function values, indicating pronounced reactivity. These insights can be further complemented using the dual descriptor Δf_k^0, which comprehensively measures electrophilic and nucleophilic reactivity.

For instance, in the monomer, atom 2C displays a high f_k^+ value, indicating it is prone to electrophilic attacks, while atom 9O has a substantial f_k^- value, suggesting it is susceptible to nucleophilic attacks. Similarly, atom 25O displays a significant f_k^+ value in the dimer compound, indicating its susceptibility to electrophilic attacks, while atom 32H has a high f_k^- value, suggesting its proneness to nucleophilic attacks, as presented in Figure 9. Understanding the reactivity patterns indicated by the Fukui function analysis can aid in designing and optimizing chemical processes.

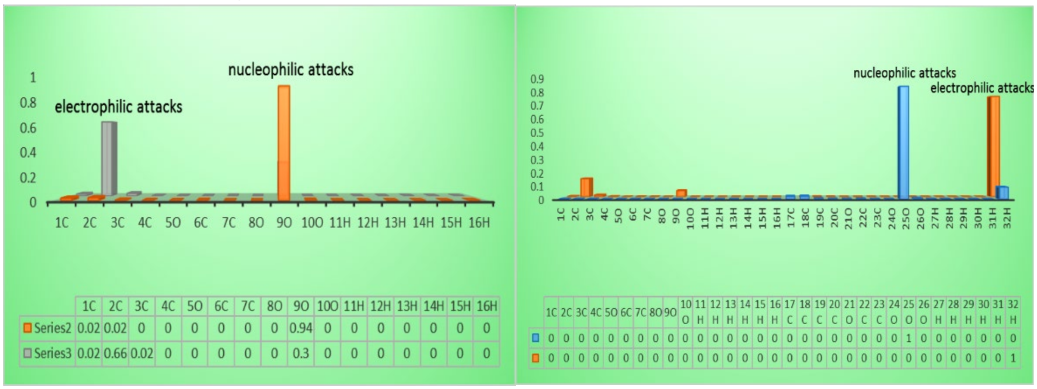

Figure 9. The active site predicted using the Fukui function for mono and dimeric compound

3.12. MM-GBSA simulations

This study explored the binding energy and interaction profiles of three protein receptors. Notably, 1HD2 exhibited substantial binding energy of -30.179 Kcal/mol, emphasizing a robust ligand-protein interaction, as shown in Figure 10 [42]. The energetic components, Evdw (-11.991) and Ecoul (-11.471) suggested a balanced contribution of van der Waals and electrostatic forces. The docking score of -5.0 reinforced the favorable binding, indicating a strong ligand-protein complex formation. Interactions were characterized by hydrogen bonds with GLY46, CYS47, ARG86, ALA90, GLY92, LYS93, VAL94, and hydrophobic interactions involving PRO40, LEU116, PHE120, and THR147. Additionally, 3AL4 and 3H4K displayed lower binding energies of -23.366 Kcal/mol and -23.087 Kcal/mol, respectively. While 3AL4 exhibited hydrogen bonds with Ser 295, Nag 606, and Glu 40, coupled with hydrophobic interactions with Leu 296, 3H4K displayed hydrogen bonds with Ala 470, Thr 472, Cys 159, and Thr 442, alongside hydrophobic interactions with Leu 441. These findings provide valuable insights into the potential drug-target interactions and contribute to understanding molecular dynamics in ligand binding to protein receptors, as represented in Figures S1 and S2 [43]. Further experimental validation is essential to corroborate these, summarized in Table 7.

The potential energy is calculated as -2744.233 kcal/mol using the OPLS3e force field. The root mean square (RMS) derivative is 0.092. The low RMSD indicates that the molecule does not change its shape very much when charged, which is essential for efficient charge transport. The maximum derivative is 1.157, reflecting the stability of the energy optimization. The study dissects energy contributions, including stretch energy, bend energy, LJ-14 energy, El-14 energy, van der Waals, electrostatic, and dihedral energy.

Table 7. Simulated binding affinities of the title compound with 1HD2, 3AL4 and 3H4K revealed additional interaction profiles

Receptor	Binding Energy (Kcal/mol)	Evdw	Ecoul	Docking Score	nhbond	Residual Interactions
1HD2	-30.179	-11.991	-11.471	-5.0	4	HBond-GLY46,CYS47, ARG86, ARG86, ALA90, GLY92, LYS93, VAL94; Hydrophobic-PRO40, LEU116, PHE120, THR147
3AL4	-23.366	-11.144	-12.222	-3.93	3	Hbond-Ser 295, Nag 606, Glu 40; Hydrophobic-Leu 296
3H4K	-23.087	-14.005	-9.081	-4.81	4	Hbond-Ala 470, Thr 472, Cys 159, Thr 442; Hydrophobic-Leu 441

Table 8. Predicted energies obtained through MM-GBSA simulation of the ligand-protein complex

Property	Value	Property	Value
Prime MMGBSA ligand efficiency	-2.494	Ligand Energy	11.86
Prime MMGBSA ligand efficiency sa	-3.741	Ligand Coulomb	13.23
Prime MMGBSA ligand efficiency ln	-7.552	Ligand Covalent	-3.28
		Ligand Lipo	-0.13
		Ligand Solv GB	-7.72
MMGBSA dG Bind	-27.31	Ligand vdW	9.75
MMGBSA dG Bind Coulomb	-22.03	Receptor Energy	-23530.59
MMGBSA dG Bind Hbond	-1.39	Receptor Coulomb	-17604.95
MMGBSA dG Bind Lipo	-4.81	Receptor Covalent	2098.88
MMGBSA dG Bind Packing	-0.01	Receptor Hbond	-329.88
MMGBSA dG Bind Solv GB	16.67	Receptor Lipo	-1225.50
MMGBSA dG Bind vdW	-15.74	Receptor Packing	-23.75
		Receptor Solv GB	-3537.16
		Receptor vdW	-2856.82
Complex Energy	-23543.66	Complex Lipo	-1230.44
Complex Coulomb	-17613.92	Complex Packing	-23.75
Complex Covalent	2097.74	Complex Solv GB	-3527.84
Complex Hbond	-331.28	Complex vdW	-2862.77

In the MM-GBSA analysis and as listed in Table 8, the Prime MMGBSA method was employed to evaluate ligand efficiency and various energetic contributions in the ligand-receptor complex. The ligand efficiency parameters revealed negative values: Prime MMGBSA ligand efficiency (-2.494), Prime MMGBSA ligand efficiency sa (-3.741), and Prime MMGBSA ligand efficiency ln (-7.552), suggesting favorable interactions. The MMGBSA dG Bind indicated a total binding free energy of -27.31 kcal/mol, predominantly contributed by Coulombic interactions (-22.03 kcal/mol), van der Waals forces (-15.74 kcal/mol), and solvation energy (16.67 kcal/mol). Individual energy components for ligands and receptors were also analyzed. Ligand energy was 11.86 kcal/mol, with significant contributions from Coulombic (13.23 kcal/mol) and van der Waals (9.75 kcal/mol) forces. Receptor energy was -23530.59 kcal/mol, mainly driven by Coulombic (-17604.95 kcal/mol) and van der Waals (-2856.82 kcal/mol) interactions. The complex energy (-23543.66 kcal/mol) mirrored the receptor energy, suggesting a well-stabilized ligand-receptor complex. Notably, covalent interactions contributed marginally to the binding free energy, with Ligand Covalent (-3.28 kcal/mol), Receptor Covalent (2098.88 kcal/mol), and Complex Covalent (2097.74 kcal/mol). These comprehensive energy profiles provide valuable insights into the energetics of ligand-receptor interactions, paving the way for a deeper understanding of the molecular dynamics governing complex formation [44].

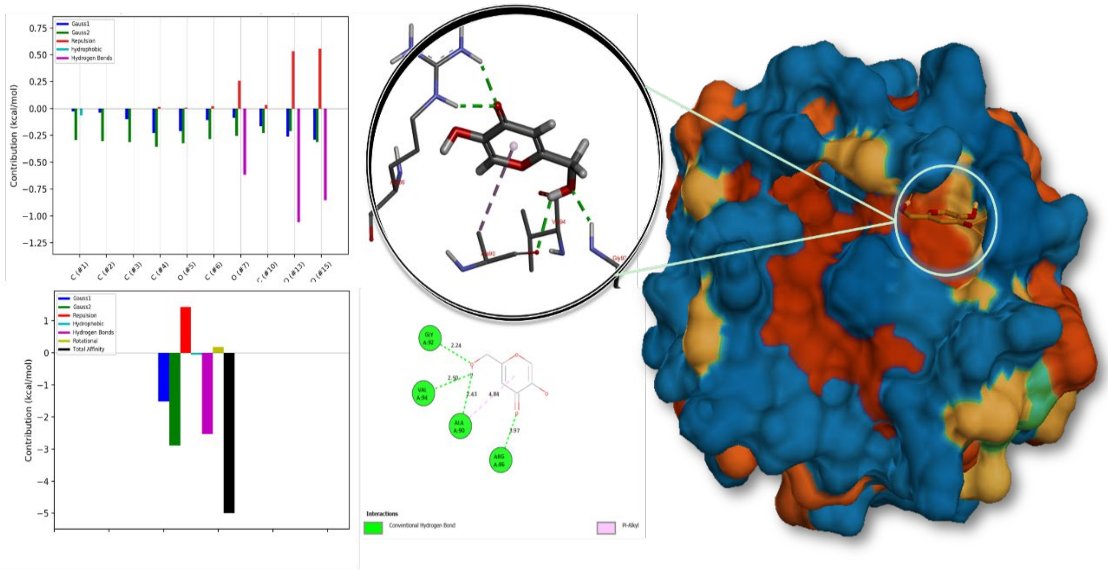

Figure 10. Ligand-protein (1HD2) interactions and H-bond, hydrophobic surface maps

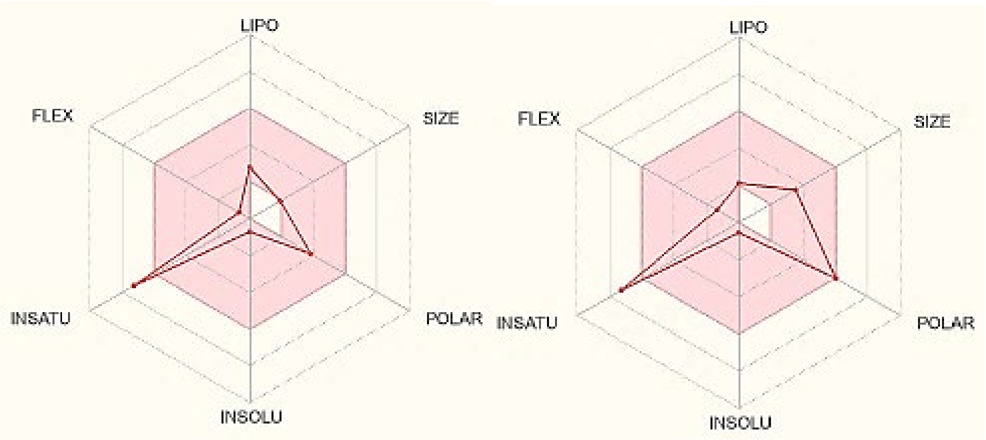

Figure 11. Drug-likeness of monomer and dimer molecule

Table 9. Drug-likeness Drug-likeness & Accessibility properties of monomer and dimer compound

Properties	Monomer	Dimer
Physicochemical Properties		
Molecular weight (MW) (g/mol)	142.11	284.22
#Rotatable bonds	1	2
H-bond acceptors	4	8
H-bond donors	2	5
MR	33.13	67.55
TPSA	70.67	129.59
Bioavailability Score	0.55	0.56
Lipophilicity		
iLOGP (Log Po/w)	1.12	0
Water Solubility		

Class	Very soluble	Very soluble
Pharmacokinetics		
GI absorption	High	High
BBB permeant	No	No
P-gp substrate	No	No
CYP1A2 inhibitor	No	No
CYP2C19 inhibitor	No	No
CYP2C9 inhibitor	No	No
CYP2D6 inhibitor	No	No
CYP3A4 inhibitor	No	No
log Kp (cm/s)	-7.62	-9.3
Drug-likeness & Accessibility		
Lipinski	0	0
Ghose	3	1
Veber	0	0
Egan	0	0
Muegge	1	0
Medicinal chemistry		
PAINS alerts	0	0
Brenk alerts	0	0
Leadlikeness	1	0
Synthetic Accessibility	2.53	3.46

3.13. Pharmacokinetic analysis

The pharmacokinetic parameters of a monomeric and its dimeric show significant differences, with the dimer exhibiting a molecular weight of 284.22 g/mol. There was an increased total polar surface area of 129.59 compared to the monomer's 70.67 and a rise in the number of hydrogen bond acceptors and donors from 4 to 8 and 2 to 5, respectively. The dimer also demonstrates a slightly lower Wildman-Crippen LogP and a reduced Incremental LogP, indicating a decrease in lipophilicity. Both molecules are classified as "Very soluble," with high gastrointestinal absorption and no blood-brain barrier permeation [45]. Notably, the dimer exhibits fewer violations in Ghose's, Muegge's, and Leadlikeness filters and, therefore, has better drug-likeness despite having a higher synthetic accessibility score (3.46) than the monomer (2.53) as shown in Table 9. As Figure 11, the observed differences highlight the potential impact of dimerization on molecular properties, such as reactivity, solubility, and drug-likeness, which necessitates further experimental validation for a comprehensive understanding of their pharmacokinetic behavior.

3.14. PASS activity spectrum

Predictions of biological activities for various compounds based on Pa and Pi values from the PASS online tool. Notable predictions include a compound with a high probability (Pa: 0.940) of inhibiting Gluconate 2-dehydrogenase, suggesting a potential role in metabolic pathways. Additionally, there are compounds predicted to be Apoptosis Agonists (Pa: 0.907), Anaphylatoxin Receptor Antagonists (Pa: 0.880), and Ubiquinol-cytochrome-c Reductase Inhibitors (Pa: 0.856), each indicating specific biological activities with high probabilities. These predictions offer insights into potential pharmacological properties.

Apoptosis (programmed cell death) is a natural process crucial for maintaining cellular balance. Compounds that agonize apoptosis could be explored in cancer research, as promoting programmed cell death in cancer cells is a common therapeutic strategy. Compounds predicted to be Apoptosis Agonists (Pa: 0.907). Anaphylatoxin receptors are part of the immune system. Antagonists may have applications in inflammatory conditions or autoimmune diseases where immune responses are dysregulated. Compounds predicted to be Anaphylatoxin Receptor Antagonists (Pa: 0.880). Compounds inhibiting the enzyme ubiquinol-cytochrome-c reductase could have implications in mitochondrial dysfunction-related disorders, as this enzyme is part of the electron transport chain in mitochondria. Compounds predicted to be Ubiquinol-cytochrome-c Reductase Inhibitors (Pa: 0.856). Inhibitors of sugar-phosphatase could be explored in conditions related to abnormal sugar metabolism, such as diabetes or metabolic syndrome—compounds with a high probability of inhibiting sugar-phosphatase. The enzyme aspulvinone dimethylallyltransferase is involved in the biosynthesis of secondary metabolites. Compounds inhibiting it might have applications in antimicrobial or antifungal research due to the role of secondary metabolites in defence mechanisms in organisms. Compounds predicted to be Aspulvinone Dimethylallyltransferase Inhibitors are presented in Table 10.

3.15. Optoelectric investigation

In this analysis, the optoelectronic properties of a material were investigated, providing valuable insights into its electronic behavior and potential applications in electronic devices. The oxidation potential was 1.737067 eV, representing the energy required for electron removal during an oxidation process [46]. Conversely, the reduction potential was observed at -2.252196 eV, indicating the energy released during electron addition in a reduction reaction. The T1S0 RMSD (Root Mean Square Deviation) was calculated to be 0.045739 Å, providing information on the structural variation between the first singlet excited state (S1) and the ground state (S0).

The material exhibited an absorption peak (λ_{max}) at 259 nm, corresponding to the wavelength of maximum absorbance. The corresponding molar absorptivity (ε_{max}) was measured at 364, indicating the material's ability to absorb light efficiently. The hole-related properties included a hole reorganization energy of 0.542495 eV, a small polaron stabilization energy of 0.257635 eV, and a hole extraction potential of 7.844057 eV. Additionally, various ionization energies for holes were determined, including vertical ionization energy (8.386552 eV), adiabatic ionization energy (8.128917 eV), and neutral stabilization energy (0.28486 eV).

Similarly, electron-related properties comprised an electron reorganization energy of 1.001924 eV, a small polaron stabilization energy of 0.478334 eV, and an electron extraction potential of 0.015414 eV. Electron ionization energies, including vertical (1.017338 eV), adiabatic (0.539004 eV), and neutral stabilization energy (0.52359 eV), were also determined. These optoelectronic characteristics collectively provide a comprehensive understanding of the material's electronic structure, aiding in assessing its suitability for various electronic applications.

In Table 11, Quantum chemical calculations were employed to elucidate the optoelectronic properties of the molecular system. Key parameters investigated include oxidation and reduction potentials, absorption spectra, and charge reorganization energies. The oxidation potential is determined to be 1.737067 eV, representing the energy required to remove an electron from the molecule. The reduction potential is -2.252196 eV, signifying the energy needed to add an electron to the molecule. Hole and electron reorganization energies are 0.542495 eV and 1.001924 eV, respectively. The high oxidation potential, a low reduction potential, a low T1S0 RMSD, a λ_{max} in the UV region, a low hole reorganization energy, and a low hole extraction potential provide insights into charge transfer processes within the molecule. This study's optoelectronic properties and excited state characteristics give a comprehensive understanding of the molecular system's electronic behavior.

Table 11. Optoelectronic properties of the title compound

Oxidation Potential (eV)	1.737067
Reduction Potential (eV)	-2.252196
T1S0 RMSD (Angstrom)	0.045739
λ_{max} (nm)	259
ε_{max} (nm)	364
Hole Reorganization Energy (eV)	0.542495
Hole Small Polaron Stabilization Energy (eV)	0.257635
Hole Extraction Potential (eV)	7.844057
Hole Vertical Ionization Energy (eV)	8.386552
Hole Adiabatic Ionization Energy (eV)	8.128917

Hole Neutral Stabilization Energy (eV)	0.28486
Electron Reorganization Energy (eV)	1.001924
Electron Small Polaron Stabilization Energy (eV)	0.478334
Electron Extraction Potential (eV)	0.015414
Electron Vertical Ionization Energy (eV)	1.017338
Electron Adiabatic Ionization Energy (eV)	0.539004
Electron Neutral Stabilization Energy (eV)	0.52359

4. Conclusions

Utilizing all the studies with the B3LYP/6-311++G(d,p) method effectively examines a compound's molecular geometry, leading to the identification of stable bond lengths and essential structural properties. Through the use of various analytical techniques, including vibrational spectral analysis, UV-visible, FT-IR, NMR spectra analysis, GCRD, NBO, MEP analysis, surface distance projection and Hirschfeld maps, Mulliken charges, thermodynamic properties, Fukui function, MM-GBSA simulations, pharmacokinetic analysis, and PASS activity spectrum predictions, the study provides valuable insights into the compound's electronic behavior and potential biological activities. Such findings are crucial for understanding molecular interactions and designing efficient drugs for therapeutic applications with molecule.

References

[1]Chakrabarti, S. S., Saso, L., Bala, S., Saha, S., Profumo, E., Buttari, B., & Chakrabarti, S. (2024). Role of oxidative stress in the pathogenesis of metabolic syndrome. In Metabolic Syndrome (pp. 143-156).

[2]Moretto, J. G., Vargas, J. E., da Silva, J. S., Pasinato, A. Z., Kunz, J. L., Marengo, P., & Barcelos, R. P. (2024). A Novel Multi-Supplement Based on Guarana, Selenium, and L-Carnitine Reduces Organ-Specific Oxidative Stress But Not Oxidative Stress-Induced Anxiety. Revista Brasileira de Farmacognosia, 1-9.

[3]Al Ati, G., Chkirate, K., El-Guourrami, O., Chakchak, H., Tüzün, B., Mague, J. T., & Essassi, E. M. (2024). Schiff base compounds constructed from pyrazole–acetamide: Synthesis, spectroscopic characterization, crystal structure, DFT, molecular docking and antioxidant activity. Journal of Molecular Structure, 1295, 136637.

[4]Aytemir MD, Karakaya G, Ekinci D. Kojic acid derivatives: INTECH Open Access Publisher; 2012.

[5]Rho HS, Lee CS, Ahn SM, Hong YD, Shin SS, Park Y-H, et al. (2011). Studies on tyrosinase inhibitory and antioxidant activities of benzoic acid derivatives containing kojic acid moiety. Bulletin of the Korean Chemical Society. 32(12):4411-4.

[6]Saeedi, M., Morteza-Semnani, K., Akbari, J., Rahimnia, S. M., Babaei, A., Eghbali, M., & Omidi, M. (2023). Eco-friendly preparation, characterization, evaluation of anti-melanogenesis/antioxidant effect and in vitro/in vivo safety profile of kojic acid loaded niosome as skin lightener preparation. Journal of Biomaterials Science, Polymer Edition, 1-29.

[7]Mohammadsadeghi, N., Mahdavi, A., Saadati, F., & Mohammadi, F. (2023). In silico and in vitro studies of novel derivatives of tyrosol and raspberry ketone as the mushroom tyrosinase inhibitors. Food Chemistry, 424, 136413.

[8]Kubaib, A., Imran, P. M., & Basha, A. A. (2022). Applications of the Vienna Ab initio simulation package, DFT and molecular interaction studies for investigating the electrochemical stability and solvation performance of non-aqueous NaMF6 electrolytes for sodium-ion batteries. Computational and Theoretical Chemistry, 1217, 113934.

[9]Kamat, V., Barretto, D. A., Poojary, B., Kumar, A., Patil, V. B., & Hamzad, S. (2024). In vitro α-amylase and α-glucosidase inhibition study of dihydropyrimidinones synthesized via one-pot Biginelli reaction in the presence of a green catalyst. Bioorganic Chemistry, 143, 107085.

[10]Filimonov, D. A., & Poroikov, V. V. (1996). PASS: Computerized prediction of biological activity spectra for chemical substances. Bioactive Compound Design: Possibilities for Industrial Use, 47-56.

[11]Gloriozova, T. A., Filimonov, D. A., Lagunin, A. A., & Poroikov, V. V. (1998). Evaluation of computer system for prediction

of biological activity PASS on the set of new chemical compounds. Chim.-Pharm. J.(Rus), 32(12), 32-39.

[12]Poroikov, V., & Filimonov, D. (2001). Computer-aided prediction of biological activity spectra. Application for finding and optimization of new leads. Rational Approaches to Drug Design, 403-407.

[13]Armaković, S., Armaković, S. J., & Koziel, S. (2017). Optoelectronic properties of curved carbon systems. Carbon, 111, 371-379.

[14]Stuart, J. G., & Jebaraj, J. W. (2023). Synthesis, characterisation, in silico molecular docking and DFT studies of 2, 6-bis (4-hydroxy-3-methoxyphenyl)-3, 5-dimethylpiperidin-4-one.

[15]Darugar, V., Vakili, M., Tayyari, S. F., & Kamounah, F. S. (2021). Validation of potential energy distribution by VEDA in vibrational assignment some of β-diketones; comparison of theoretical predictions and experimental vibration shifts upon deutration. Journal of Molecular Graphics and Modelling, 107, 107976.

[16]Bhavani, R., Kanagathara, N., Marchewka, M. K., Janczak, J., Senthilkumar, K., & Azam, M. (2024). Single crystal analysis and DFT studies of the novel hybrid material-based on 2-hydroxypyridine and selenic acid. Results in Chemistry, 7, 101239.

[17]Saikia, J., Devi, T. G., & Karlo, T. (2023). DFT calculations, spectroscopic investigations, and molecular docking study of Methylprednisolone with some selective cancer proteins. Materials Today: Proceedings.

[18]Basha, A. A., Kubaib, A., & Azam, M. (2024). Exploring the antiviral potency of γ-FP and PA compounds: Electronic characterization, non-covalent interaction analysis and docking profiling with emphasis on QTAIM aspects. Computational and Theoretical Chemistry, 1231, 114412.

[19]Hadi, H., Chouchen, B., Nasr, S., Bouzid, G., Chérif, I., Basha, A., & Ayachi, S. (2024). Exploring High-Performance Functionalized Corannulene Dimers: A DFT-Based Investigation for Novel Photovoltaic Applications. Synthetic Metals, 117543.

[20]Lu, T., & Chen, F. (2012). Multiwfn: A multifunctional wavefunction analyzer. Journal of computational chemistry, 33(5), 580-592.

[21]Kubaib, A., & Imran, P. M. (2023). Fabrication of Li, Na and K electrolytes with doping elements for improved efficiency based on MOT and symmetry. Journal of the Indian Chemical Society, 100(1), 100804.

[22]Mason, J. S., Good, A. C., & Martin, E. J. (2001). 3-D pharmacophores in drug discovery. Current pharmaceutical design, 7(7), 567-597.

[23]Basha, A. A., Khan, F. L. A., Muthu, S., Imran, P. M., & Kubaib, A. (2023). Dielectric relaxation, dipole moment, electronic characterization and non-covalent interaction behavior of valeramide and halo-phenol in non-polar liquid: A density functional theory-based approach. Journal of Molecular Liquids, 370, 121027.

[24]Saranya, G., Devendraprasad, K., Shanmugapriya, P., & Bhuvaneshwari, N. (2023). DFT calculations, molecular docking, in vitro antimicrobial and antidiabetic studies of green synthesized Schiff bases: as Covid-19 inhibitor. Journal of biomolecular structure & dynamics, 1-18.

[25]Daina, A., Michielin, O., & Zoete, V. (2017). SwissADME: a free web tool to evaluate pharmacokinetics, drug-likeness and medicinal chemistry friendliness of small molecules. Scientific reports, 7(1), 42717.

[26]Release, S. (2018). 4: Jaguar. Schrödinger, LLC, New York, NY.

[27]Shivakumar, D., Williams, J., Wu, Y., Damm, W., Shelley, J., & Sherman, W. (2010). Prediction of absolute solvation free energies using molecular dynamics free energy perturbation and the OPLS force field. Journal of chemical theory and computation, 6(5), 1509-1519.

[28]Fatima, A., Khanum, G., Sharma, A., Siddiqui, N., Muthu, S., Butcher, R. J., & Javed, S. (2022). Synthesis, single crystal X-ray, DFT, Hirshfeld surface and molecular docking studies of 9-(2, 4-dichlorophenyl)-4a-hydroxy-tetramethyl-octahydro-1H-xanthene-1, 8 (2H)-dione. Journal of Molecular Structure, 1268, 133613.

[29]Yurdakul, Ş., & Polat, T. (2010). FT-IR, FT-Raman spectra, density functional computations of the vibrational spectra and molecular geometry of 2-

hydroxyquinoxaline. Journal of Molecular Structure, 963(2-3), 194-201.

[30]Ganesan, T. S., Elangovan, N., Vanmathi, V., Sowrirajan, S., Chandrasekar, S., Murthy, K. S., & Thomas, R. (2022). Spectroscopic, Computational (DFT), Quantum mechanical studies and protein-ligand interaction of Schiff base 6, 6-((1, 2-phenylenebis (azaneylylidene)) bis (methaneylylidene)) bis (2-methoxyphenol) from o-phenylenediamine and 3-methoxysalicylaldehyde. Journal of the Indian Chemical Society, 99(10), 100713.

[31]Hilary, H. J. L., Prabakar, P. J., Vijayakumar, G., Rejith, S. G., Divya, J., & Sathana, V. (2023). Investigation on the growth, characterization and computational analysis of 2-Amino-2-thiazoline single crystals. Chemical Physics Impact, 6, 100187.

[32]Rifana, B. A., Prasana, J. C., Muthu, S., Anuradha, A., & Irfan, A. (2023). Experimental spectroscopy, eco-friendly solvents effect on transitions, reactive sites and biological research on methyl gallate–MTT assay (cytotoxicity). Journal of Molecular Liquids, 371, 121092.

[33]Abirami, V., Pari, S., Sumithanandhi, S., Muthupandi, S., Selvam, L. A., & Prathap, S. (2023, May). Quantum chemical studies on the molecular structure and optical properties of 2-amino-5-bromo benzaldehyde compound based on DFT calculations. In AIP Conference Proceedings (Vol. 2770, No. 1). AIP Publishing.

[34]Mishma, J. C., Jothy, V. B., Narayana, B., Kodlady, S. N., Alharbi, N. S., Abbas, G., & Muthu, S. (2023). Synthesis, DFT, solvent effect and biological attributes of NLO active 4-bromo-2-((2-(2, 4-Dinitrophenyl) hydrazono) methyl) phenol-Potent drug anti-brain cancer. Journal of Molecular Structure, 1289, 135839.

[35]Reeda, V. J., Divya, P., Suja, R., Rathika, A., & Jothy, V. B. (2023). Synthesis, Spectroscopic Investigations, Topological Non-Covalent Interactions, Chemical Reactivity, Molecular Docking and Molecular Dynamic Simulation on Piperazine Succinate-A Potential Antimicrobial Compound. Journal of Molecular Structure, 136179.

[36]Basha, A. A., Khan, F. L. A., Muzammil, P., & Fasiuddin, G. S. (2022). Dielectric relaxation and dipole moment studies of hydrogen bonded complexes for enanthamide and valeramide with halogenated phenols using J-band microwave frequency. Materials Research Express, 9(7), 075303.

[37]Selvakumaran, M., Imran, P. M., Kubaib, A., Azam, M., Basha, A. A., & Al-Resayes, S. I. (2024). Investigations into the anti-inflammatory and anti-diabetic activity of newly synthesized derivatives of 4AP2BOB utilizing DFT, molecular docking and spectroscopic characterization. Journal of Molecular Liquids, 123983.

[38]Chamorro, E., Guerra, C., Ayarde-Henríquez, L., Duque-Noreña, M., Pérez, P., & Rincón, E. (2023). New insights from a bonding evolution theory based on the topological analysis of the electron localization function. Chemical Reactivity, 465-481.

[39]Yadav, N. P., Vishwkarma, A. K., Maddheshiya, A. K., Yadav, T., Moharana, S., Kumar, R.,& Tripathi, P. K. (2023). Molecular geometries, vibrational spectra and electronic properties of biphenyl nematic liquid crystals: a quantum chemical analysis. Molecular Physics, e2210957.

[40]M. Yeo , P.M. Niamien , E.B.A. Bilé, A. Trokourey , (2018). Thiamine Hydrochloride as a Potential Inhibitor for Aluminium Corrosion in 1.0 M HCl: mass Loss and DFT Studies, Journal of Computational Methods in Molecular Design 8 (1) 13–25.

[41]Alam, A., Jawaid, T., & Alam, P. (2021). In vitro antioxidant and anti-inflammatory activities of green cardamom essential oil and in silico molecular docking of its major bioactives. Journal of Taibah University for Science, 15(1), 757-768.

[42]Noumi, E., Ahmad, I., Adnan, M., Merghni, A., Patel, H., Haddaji, N., & De Feo, V. (2023). GC/MS Profiling, Antibacterial, Anti-Quorum Sensing, and Antibiofilm Properties of Anethum graveolens L. Essential Oil: Molecular Docking Study and In-Silico ADME Profiling. Plants, 12(10), 1997.

[43]Mujafarkani, N., Ojong, M. A., Ahamed, A. J., Benjamin, I., Ngana, O. C., Akor, F. O.,& Louis, H. (2023). Spectroscopic characterization, polar solvation effects, DFT studies, and the antiviral inhibitory potency of a novel terpolymer based on p-Phenylenediamine–Guanidine–Formaldehyde (PGF) ligand. Journal of Molecular Structure, 136049.

[44]Alzahrani, A. Y. A., Ullah, H., Bhat, M. A., Rahim, F., Al-Wesabi, E. O., & Alanazi, T. Y. (2024). Design, synthesis, in vitro acetylcholinesterase, butyrylcholinesterase activities, and in silico molecular docking study of oxindole-oxadiazole hybrid analogues. Journal of Molecular Structure, 1299, 137167.

[45]Praveen, M., Ullah, I., Buendia, R., Khan, I. A., Sayed, M. G., Kabir, R., & Yaseen, M. (2024). Exploring Potentilla nepalensis Phytoconstituents: Integrated Strategies of Network Pharmacology, Molecular Docking, Dynamic Simulations, and MMGBSA Analysis for Cancer Therapeutic Targets Discovery. Pharmaceuticals, 17(1), 134.

[46]Tomar, R., Naaz, T., Pandit, S., Mathuriya, A. S., & Jadhav, D. A. (2024). Exploring the potential of metal-doped perovskite-oxides as oxygen reduction catalyst for enhancing the performance of microbial desalination cells. Fuel, 356, 129451.